Charge and magnetic ordering near inhomogeneities in monolayer $2H$-$NbSe_2$

Buddhadeb Debnath,[1,2] Mayank Gupta,[2,3] B. R. K. Nanda,[2,3] and Shantanu Mukherjee[1,2,4]
[1]*Department of Physics, Indian Institute of Technology Madras, Chennai 600036, India*
[2]*Center for Atomistic Modelling and Materials Design, IIT Madras, Chennai 600036, India*
[3]*Condensed Matter Theory and Computational Lab, Department of Physics, IIT Madras, Chennai 600036, India*
[4]*Quantum Centres in Diamond and Emergent Materials (QCenDiem)-Group, IIT Madras, Chennai, Tamil Nadu 600036, India*

(Received 4 March 2024; revised 14 May 2024; accepted 15 May 2024; published 28 May 2024)

Recent interest in two-dimensional dichalcogenide materials is compounded by an anisotropic spin-orbit coupling (SOC) and proximity to competing orders like charge density wave (CDW), spin density wave, and superconductivity. In monolayer $2H$-$NbSe_2$, the low-energy electronic structure is influenced by the presence of an Ising SOC, the formation of a 3Q CDW order ($Q = 2/3\Gamma M$), and a nontrivial topology that includes the electronic environment near impurities and edges. Scanning tunneling microscopy (STM) experiments have observed a transition from a 3Q CDW order on the surface to a 1Q charge stripe order near its edges, and the presence of impurities leads to a nontrivial dependence of superconducting transition temperature on impurity concentration. First-principle calculations also predict that the material will have strong paramagnetic fluctuations and lie close to a magnetic instability. In this work, we use a realistic multiorbital model derived from density functional theory (DFT) calculations, and we implement it on a real-space Hamiltonian to study the interplay between Ising SOC, charge density wave, and a proximate magnetic order. We find that near inhomogeneities like impurities and edges, such an interplay can lead to interesting local charge and magnetic signatures that are in agreement with experimental observations such as 1Q CDW order near the material edge. We also find that due to an interplay with the underlying CDW state, the local electronic order near certain impurity sites in monolayer $2H$-$NbSe_2$ can show a twofold-symmetric pattern. Finally, we propose that strong spin fluctuations can lead to the formation of local magnetic order near disorder and influence the electronic properties of this material.

DOI: 10.1103/PhysRevB.109.174212

I. INTRODUCTION

$2H$-$NbSe_2$ is a material that draws research interest due to the nature of an observed 3Q charge density wave (CDW) and superconducting order both in the bulk and monolayer materials [1–9]. In bilayer bulk $2H$-$NbSe_2$, a Fermi surface nesting is found to be relatively weak, and the strong electron-phonon (e-ph) coupling has been proposed to play a major role in the formation of the 3Q CDW state [10,11]. The emergent charge order observed in the monolayer material differs from the bulk material in some significant ways. The CDW transition temperature increases from 33.5 K (bulk) to 145 K (monolayer) [1], whereas the superconducting transition temperature decreases with lowering layer numbers [1,4,12]. Unlike bulk $2H$-$NbSe_2$, the monolayer material breaks inversion symmetry and develops an Ising spin orbit coupling (SOC) and strongly enhanced paramagnetic fluctuations revealed by first-principles calculations [7]. These deviations in the electronic properties due to the reduction in the number of layers provide us with an opportunity to understand how the 3Q CDW state interacts with Ising SOC and enhanced magnetic fluctuations both in the homogeneous material and in the presence of disorder.

To understand the origin of CDW in $2H$-$NbSe_2$, it is important to understand the role of e-ph coupling in the formation of CDW [10,11,13]. For bulk $2H$-$NbSe_2$, the low-energy bands are dominated by $4d_{z^2}$ orbitals of Nb atoms of two different layers. The orbital overlap between these interlayer $4d_{z^2}$ orbitals leads to an e-ph coupling matrix element that is found to be directly proportional to the electronic band velocity. The calculated charge susceptibility cannot explain the 3Q CDW wave vector at $\boldsymbol{Q} = 2/3\Gamma M$ from a purely nesting driven scenario, and a contribution from a momentum-dependant e-ph interaction is required to obtain a susceptibility peak at the expected CDW wave vector [10,11].

The structure of monolayer $2H$-$NbSe_2$ is devoid of a bilayer coupling but is believed to show rich physics due to the presence of a broken inversion symmetry [14–16]. The broken inversion symmetry combined with in-plane mirror symmetry leads to an Ising spin-orbit coupling [15,17,18]. The spin valley locking resulting from Ising SOC causes electron spins to align in the out-of-plane direction, making the material more resistant to the effects of an external in-plane magnetic field. For example, this leads to a significant enhancement in the in-plane upper critical field within the superconducting state [17,19].

Previous theoretical study of charge ordering in monolayer $2H$-$NbSe_2$ with density functional theory (DFT) shows a broadened maxima in the real part of noninteracting susceptibility within the range $2/5\Gamma M$–$4/5\Gamma M$ instead of a peak at the CDW wave vector [14,21–24]. With the *GW* approximation, the peaks do not show any significant change [14]. It is also found that the presence of atomic SOC does not lead to any noticeable change in the susceptibility [14]. In a recent study considering a single-band model of monolayer $2H$-$NbSe_2$, the susceptibility peak was found to appear far away from the

experimentally observed charge-order peak and strengthens in the presence of momentum-dependent e-ph coupling [25,26]. Therefore, it would be interesting to study the role of e-ph coupling on charge susceptibility within a realistic multiorbital model and study the effect of variation in Ising SOC and electron doping in the monolayer $2H$-$NbSe_2$.

It has been argued that the Ising SOC also allows for nontrivial topological properties, and exotic particles like Majorana bound states (MBSs) could form in these systems [15]. Within the superconducting phase, the presence of a Yu-Shiba-Rusinov (YSR) state is found to be effected by the presence of the CDW order [27,28]. Therefore, the nontrivial topology combined with the presence of the 3Q CDW order is likely to lead to interesting electronic properties near impurities and at the edge of monolayer $2H$-$NbSe_2$ [2]. A recent STM experiment found that the 3Q CDW seen in the local density of states (LDOS) gets modified into a stripe 1Q CDW order near the edge [2]. To understand the origin of the 1Q CDW formation, we utilize a six-orbital Hamiltonian on a real-space lattice and model the edge state CDW properties for different edge termination geometries. We find reasonable agreement both in the spatial dependence and the energy dependence of the calculated CDW in the bulk and edge states.

Apart from edge states, nonmagnetic and magnetic impurities play an important role in monolayer $2H$-$NbSe_2$. Se and Fe defects decrease the superconducting transition temperature in the case of monolayer $2H$-$NbSe_2$ [29]. In the presence of disorder, monolayer $2H$-$NbSe_2$ shows a nontrivial competition between CDW and superconductivity as well as between different types of CDW ground states [30–35]. The symmetry of the CDW state is also proposed to break under Co or Mn adsorption [30]. Our real-space calculations reveal local electronic effects in the presence of impurities due to an interplay with the underlying CDW phase. We use the Ising SOC as a tuning parameter and identify its role in the local symmetry breaking near impurity sites. In particular, we study the variations of local electronic structure at inequivalent impurity sites that are induced by the periodicity of 3Q CDW order.

Apart from the presence of charge ordering, monolayer $2H$-$NbSe_2$ has been proposed to lie close to a magnetic instability [7]. Superconductivity and ferromagnetism have been found to co-exist in the case of $NbSe_{1.85}$ for the bulk system [29]. In other transition-metal dichalcogenides, a ferromagnetic state with a significant magnetic moment of $0.25\mu_B$/Mo is found to stabilize by creating sulfur vacancies in MoS_2 [36]. Such a closely lying magnetic instability makes these monolayer materials particularly susceptible towards showing local moment formation near impurities and edges. Impurity-induced magnetism has been studied in different materials when the system is near magnetic instability [37–42]. Within our real-space self-consistent calculations, we find that a local magnetic ordering can indeed form near impurities and edges of this material, and we study how the moments are expected to spatially vary as a function of impurity strength or distance from various edge terminations.

In the following, we extract a realistic low-energy tight-binding Hamiltonian for monolayer $2H$-$NbSe_2$ from DFT calculations. The three-orbital tight-binding Hamiltonian is composed of three $4d$ orbitals of an Nb atom, although the basis is doubled due to the presence of the Ising spin-orbit coupling leading to an effective 6×6 Hamiltonian matrix. We next evaluate the multiorbital charge susceptibility and the renormalization of the susceptibility due to e-ph interactions. By utilizing Ising SOC as a tuning parameter, we show how the SOC and e-ph interaction govern the emergence of a dominant CDW peak near the 3Q wave vector. To compute the effect of local impurities and edge, we utilize a real-space model and self-consistently calculate the mean fields. The impurity-induced magnetism is studied by incorporating a Hubbard-Kanamori Hamiltonian and requiring the system to be proximate to a magnetic instability. We find that nonmagnetic impurities can induce a local magnetic moment whose coherence length depends upon the strength of the impurity potential and Coulomb interaction. We further discuss the role of Ising SOC and CDW order in localizing and enhancing the magnitude of the disorder-induced magnetic moment.

II. MODEL

Although the monolayer structure breaks inversion symmetry, the presence of a horizontal mirror plane generates an effective internal electric field in the Nb plane. The corresponding Ising SOC leads to a spin momentum locking that favors the electron spins to point along the out-of-plane z-direction. In the momentum space, the spin-orbit coupling induced band splitting leads to a $|\boldsymbol{k},\uparrow\rangle$ and $|\boldsymbol{k}',\downarrow\rangle$ spin momentum locked electronic structure.

The electronic structure of monolayer $NbSe_2$ was generated using DFT calculations. The density functional theory calculations were performed using the pseudopotential-based projector augmented wave (PAW) [43] method as implemented in the Vienna ab initio simulation package (VASP) [44]. The generalized gradient approximation (GGA) was chosen for the exchange correlation functional [45]. The Brillouin zone integration was carried out using a $12\times12\times1$, Γ-centered k-mesh. The kinetic energy cutoff for the plane-wave basis set was chosen to be 500 eV. The PAW basis functions include $5s$ and $4d$ orbitals for Nb, and $4s$ and $4p$ orbitals for Se, respectively. Spin-orbit coupling (SOC) was considered when calculating the electronic structure. The thickness of the vacuum layer in the z direction is taken to be 15 Å.

The primitive cell of monolayer $2H$-$NbSe_2$ is shown in Fig. 1(a). DFT calculations reveal that the low-energy Hamiltonian is composed of contributions from Nb $3d$ orbitals [Fig. 1(b)]. The orbital-resolved band structure, shown in Fig. 1(b), suggests that the primary contributions to the bands crossing the Fermi level are from d_{z^2}, d_{xy}, and $d_{x^2-y^2}$ orbitals of an Nb atom. From the band-structure plot in Fig. 1(b) we can also infer that the Γ-centered Fermi pocket is mostly composed of d_{z^2} orbital contributions, whereas the K- and K'-centered pockets are primarily composed of $d_{x^2-y^2}$ and d_{xy} orbitals. We develop an effective tight-binding Hamiltonian composed of the ($d_{z^2\uparrow}$, $d_{xy\uparrow}$, $d_{x^2-y^2\uparrow}$, $d_{z^2\downarrow}$, $d_{xy\downarrow}$, $d_{x^2-y^2\downarrow}$) basis (see Fig. 10 in Appendix A for a comparison between DFT electronic structure and the tight-binding Hamiltonian). The general form of the Hamiltonian relevant for monolayer

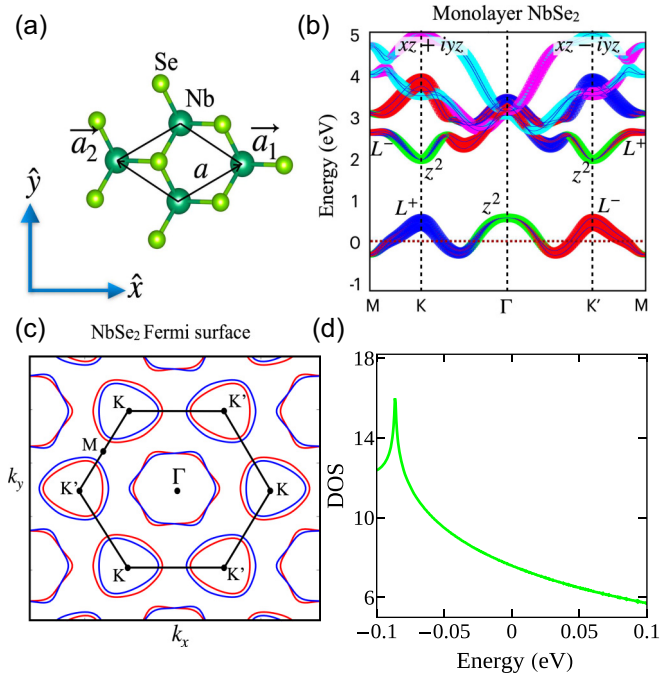

FIG. 1. (a) Primitive cell (top view), (b) low energy electronic structure. Here, L_+ and L_- is defined as $|d_{x^2-y^2}\rangle + i|d_{xy}\rangle$ and $|d_{x^2-y^2}\rangle - i|d_{xy}\rangle$ respectively [20]. (c) Fermi surface, and (d) density of state of monolayer 2H-$NbSe_2$ (in eV^{-1}).

$2H$-$NbSe_2$ is given as

$$H_{\rm TB} = \sum_{\mu,\nu,\sigma,\mathbf{k}} \xi^{\sigma}_{\mu\nu}(\boldsymbol{k}) d^{\dagger}_{\mu\sigma}(\boldsymbol{k}) d_{\nu\sigma}(\boldsymbol{k}). \tag{1}$$

The operator $d_{\mu\sigma}(\boldsymbol{k})$ $[d^{\dagger}_{\mu\sigma}(\boldsymbol{k})]$ annihilates (creates) an electron in orbital μ, spin σ, and momentum $\boldsymbol{k}$, respectively. The tight-binding parameters and their momentum dispersion are provided in Appendix A, and the extracted low-energy band structure shows good agreement with DFT results. As can be seen from Fig. 1(b), there are primarily two bands comprising the Fermi surface that lead to Fermi pockets centered at Γ, K, and K' points. The color scale represents the spin character of the resulting bands that inherently break the inversion symmetry but keep the time-reversal symmetry intact [Fig. 1(c)]. The density of states (DOS) [Fig. 1(d)] shows a peak near $\omega = -0.1$ eV originating from the energy minima between the Γ and K points, and it keeps decreasing for higher energies.

To explore the nature of CDW order in monolayer $2H$-$NbSe_2$, and to identify the role of Ising SOC, we have calculated the multiorbital charge susceptibility including the effect of an anisotropic e-ph interaction. The charge susceptibility in the orbital basis including momentum dependent e-ph coupling is given by [13]

$$\chi(\mathbf{q})^{\mu\nu}_{\gamma\delta} = -\frac{1}{N}\sum_{\mathbf{k},s,p}\left[U^{s}_{\gamma}(\mathbf{k})U^{s\star}_{\mu}(\mathbf{k})U^{p}_{\nu}(\mathbf{k}+\mathbf{q})U^{p\star}_{\delta}(\mathbf{k}+\mathbf{q})\right] \times \left(g^{s,p}_{\mathbf{k},\mathbf{k}+\mathbf{q}} g^{p,s}_{\mathbf{k}+\mathbf{q},\mathbf{k}}\right)\frac{f\left(\xi^{s}_{\mathbf{k}}\right) - f\left(\xi^{p}_{\mathbf{k}+\mathbf{q}}\right)}{\xi^{s}_{\mathbf{k}} - \xi^{p}_{\mathbf{k}+\mathbf{q}}}, \tag{2}$$

where μ, ν, γ, δ represent the orbital indices, and s, p are the band indices, each running from 1 to 6. Here, $\xi^{s}_{\mathbf{k}}$, and $U^{s}_{\gamma}(\mathbf{k})$ are the band energies and corresponding eigenvector components of the noninteracting Hamiltonian, respectively. The momentum-dependent e-ph interaction is given by $g^{s,p}_{\mathbf{k},\mathbf{k}+\mathbf{q}}$.

The e-ph interaction has been calculated using a method proposed by Varma *et al.* [13]. The model has been successfully utilized to obtain the correct dominant ordering wave vector for the 3Q CDW state observed in bulk $2H$-$NbSe_2$ [10,11]. The e-ph matrix element is given by

$$g^{s,p}_{\mathbf{k},\mathbf{k}+\mathbf{q}} = v^{s}_{\mathbf{k}}[A^{\dagger}_{\mathbf{k}} S_{\mathbf{k}} A_{\mathbf{k}+\mathbf{q}}]^{s,p} - [A^{\dagger}_{\mathbf{k}} S_{\mathbf{k}+\mathbf{q}} A_{\mathbf{k}+\mathbf{q}}]^{s,p} v^{p}_{\mathbf{k}+\mathbf{q}}, \tag{3}$$

where $v^{s}_{\mathbf{k}} = \frac{\partial \xi^{s}_{\mathbf{k}}}{\partial \mathbf{k}}$ is the electronic band velocity of the sth band [10], $A_{\mathbf{k}}$ represents the eigenvector matrix calculated at the wave vector $\mathbf{k}$, and the matrix $S_{\mathbf{k}}$ is the orbital superposition matrix [13].

A real-space analysis of charge-order physics and disorder effects in this system involves a Fourier transformation of the six-orbital momentum space Hamiltonian into the real space. The real-space Hamiltonian including the CDW order takes the form

$$H = H_0 + H_{\rm SOC} + H_{\rm CDW}, \tag{4}$$

where H_0 is given by

$$H_0 = \sum_{i,j,\mu,\nu,\sigma} t^{\mu\nu}_{ij} c^{\dagger}_{i\mu\sigma} c_{j\nu\sigma} - \mu_c \sum_{i\mu\sigma} c^{\dagger}_{i\mu\sigma} c_{i\mu\sigma}. \tag{5}$$

Here, i and j are the site indices. μ and ν are the orbital indices running from 1 to 3 representing d_{z^2}, d_{xy}, and $d_{x^2-y^2}$ orbitals, $\sigma = (\uparrow, \downarrow)$ stands for the spin index, μ_c is the chemical potential, and $c^{\dagger}_{i\mu\sigma}$ and $c_{i\mu\sigma}$ represent creation and annihilation operators of an electron at the site i for orbital μ and spin σ, respectively. The spin-orbit coupling term $H_{\rm SOC}$ is described in Appendix A. The charge-order Hamiltonian (see Appendix B for details) in real space is given by

$$H_{\rm CDW} = \sum_{\substack{\mu,\nu,\gamma,\delta,\\ j,m,\sigma}} \Delta^{m\sigma}_{\mu\nu}(\mathbf{r}_j) c^{\dagger}_{\gamma j\sigma} c_{\delta j\sigma}, \tag{6}$$

where

$$\Delta^{m\sigma}_{\mu\nu}(\mathbf{r}_j) = V_{\rm CDW} \sum_{i} \cos[\mathbf{Q}_m.(\mathbf{r}_i - \mathbf{r}_j)]\langle c^{\dagger}_{\mu i\sigma} c_{\nu i\sigma}\rangle. \tag{7}$$

Here, the index m labeling the CDW wave vector runs from 1 to 3 as we are dealing with a 3Q type of charge ordering in the system. $V_{\rm CDW}$ represents the CDW amplitude, and μ, ν, γ, δ represent the orbital indices running from 1 to 3 in a real-space Hamiltonian considered on a 33×33 lattice. The real-space Hamiltonian considered in this work assumes a site-ordered CDW gap [46,47]. Similar approximation has been considered previously for modeling 3Q CDW order in $NbSe_2$, and it provides a reasonably good agreement with the local density of states measured in STM experiments.

To study the impurity effect, we additionally include an impurity Hamiltonian term. The total Hamiltonian including the impurity term is given by

$$H = H_0 + H_{\rm SOC} + H_{\rm CDW} + H_{\rm imp}. \tag{8}$$

For a potential impurity problem, H_{imp} takes the form

$$H_{\text{imp}} = V_{\text{imp}} \sum_{\mu,\sigma} c^{\dagger}_{i,\mu,\sigma} c_{i,\mu,\sigma}, \tag{9}$$

where V_{imp} is the impurity potential strength.

To study the effect of two different types of edges, we deal with an open boundary condition along the x and y directions utilizing the Hamiltonian described in Eq. (4). If we keep the boundary open along the x direction we will get the line edge, and an open boundary along the y direction will lead to a zigzag edge.

Motivated by proposals for strong ferromagnetic fluctuations in this system, we study in some detail the nature of magnetic moment induced near impurities and edges. To model the local magnetism that could be induced near impurities and edges, we introduce a local interaction via a Hubbard-Kanamori Hamiltonian,

$$H_U = U \sum_{i,\mu} \hat{n}_{i\mu\uparrow}\hat{n}_{i\mu\downarrow} + U' \sum_{i,\mu\neq\nu} \sum_{\sigma} \hat{n}_{i\mu\sigma}\hat{n}_{i\nu\bar{\sigma}} + (U' - J) \sum_{i,\mu\neq\nu} \sum_{\sigma} \hat{n}_{i\mu\sigma}\hat{n}_{i\nu\sigma}, \tag{10}$$

where $U' = U - 2J$, and we choose $J = 0.25U$. The total Hamiltonian for this system then becomes

$$H = H_0 + H_U + H_{\text{SOC}} + H_{\text{CDW}} + H_{\text{imp}}. \tag{11}$$

Since no long-range magnetism is known to occur in this system, the Hubbard parameter is tuned close to but below the stoner value $U = U_c$. In a real-space self-consistent calculation, the mean fields including site- and orbital-resolved magnetism are then calculated both near impurities and edges to identify whether the system can locally cross the stoner criterion due to a local charge redistribution near the disorder and form magnetic puddles.

III. RESULTS

A. Charge susceptibility

We first calculate orbital-resolved charge susceptibility in the absence of e-ph coupling within the six-orbital model and an Ising spin-orbit coupling of 75 meV that provides a good agreement with the DFT generated low-energy electronic structure for monolayer $2H$-$NbSe_2$. The total physical susceptibility is shown in Fig. 2(a). In the absence of e-ph coupling, there is a broadened maximum that is significantly shifted from the experimentally observed CDW wave vector $Q = 2/3\Gamma M$. Similar to previous observations for bulk $2H$-$NbSe_2$ [10,11], this indicates that a purely nesting driven scenario cannot explain the charge-order transition in monolayer $2H$-$NbSe_2$. Note that we do find that in the absence of e-ph coupling, the charge susceptibility can be obtained at the relevant $Q = 2/3\Gamma M$ wave vector by considering a stronger Ising SOC of about 200 meV, but this would lead to deviations in agreement with DFT generated electronic structure.

We then calculate the susceptibility in the presence of e-ph coupling and light electron doping. The noninteracting susceptibility of the electron-doped material in the absence of e-ph coupling has been calculated previously [14], and our model shows quantitative agreement with these results.

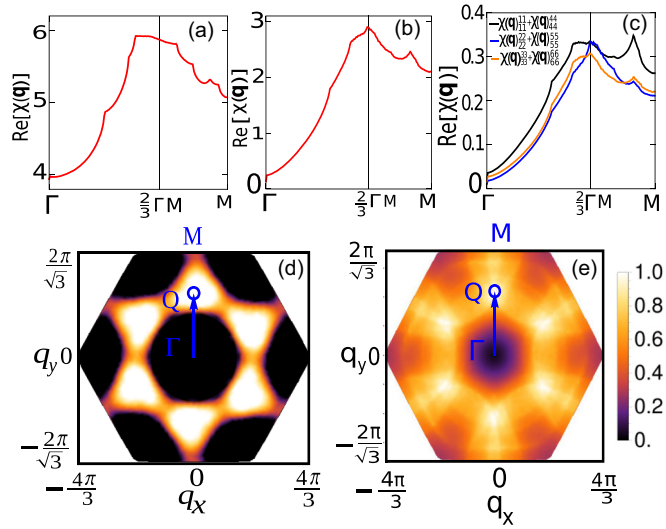

FIG. 2. Calculation of charge susceptibility in different cases. (a) Total charge susceptibility with an Ising SOC value 0.075 eV. (b) Total charge susceptibility with Ising SOC in the presence of e-ph coupling. (c) Orbital-resolved charge susceptibility for the case similar to (b). Parts (d) and (e) represent e-ph coupling magnitude and charge susceptibility, respectively, calculated over the first Brillouin zone for the case similar to (b). From the plots (b) and (e), it is clear that the total susceptibility plot shows a sharp peak at $\frac{2}{3}\Gamma M$.

In Fig. 2(d), we show the e-ph matrix element by calculating the function $\sum_{\boldsymbol{k}} |g_{k,q}|^2$. The e-ph interaction is peaked at the CDW wave vector, and its effect leads to a charge susceptibility peak at the CDW wave vector. The total charge susceptibility in the presence of e-ph coupling now shows a strongly enhanced peak at the experimentally observed CDW wave vector [see Figs. 2(b) and 2(e)]. Orbital-resolved susceptibility calculation shows that all three orbitals are contributing significantly in the CDW formation [Fig. 2(c)], although the d_{xy} and $d_{x^2-y^2}$ orbital contributions are primarily responsible for the dominant peak at the CDW wave vector. These results imply that although the Hamiltonian of monolayer $2H$-$NbSe_2$ differs from the bulk $2H$-$NbSe_2$ Hamiltonian in some important aspects, the CDW formation in both cases can be described by assuming a momentum-dependent e-ph coupling.

B. Charge density wave

The CDW transition in monolayer $2H$-$NbSe_2$ is observed at $T_c \sim 145$ K. The calculated charge-density wave for the homogeneous system is shown in Fig. 3. In Fig. 3(a), we plot the local electron density variation at a lattice site given by $\delta n_i = n_i - n$, where n_i is the computed site resolved electron occupation and n represents its average value over all sites. We find the ground-state CDW profile favors a form factor with three separate site-resolved order parameters for which a Fourier transform of the electron density shows a peak at the expected $Q = 2/3\Gamma M$ wave vector [Fig. 3(b)]. Within these sites, whereas site 1 locally preserves a sixfold rotational symmetry, site 2 locally forms a threefold-symmetric charge-density profile around it, and site 3 locally breaks even the D_{3h} point-group symmetry [Fig. 3(a)]. Although for global

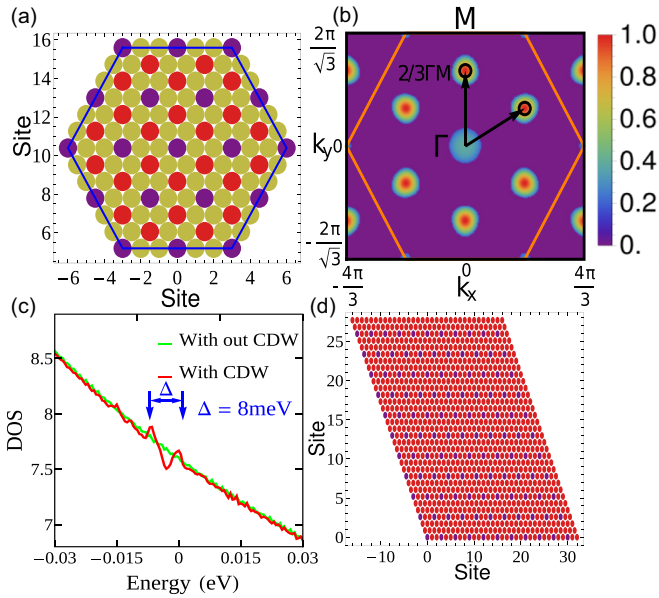

FIG. 3. (a) Self-consistently calculated real-space CDW map for $V_{\mathrm{CDW}} = 0.02\,\mathrm{eV}$. The three inequivalent electron densities in the CDW state are 1: purple with $\delta n_i = -0.02$, 2: red with $\delta n_i = 0.02$, and 3: yellow with $\delta n_i = 0$, where δn_i is the shift in electron occupation due to CDW. (b) Fourier transformation of the real-space CDW order parameter shows the peak at $\frac{2}{3}\Gamma M$, (c) total DOS showing the CDW dip around Fermi energy, and (d) LDOS map over a real-space lattice at $\omega = 20\,\mathrm{meV}$.

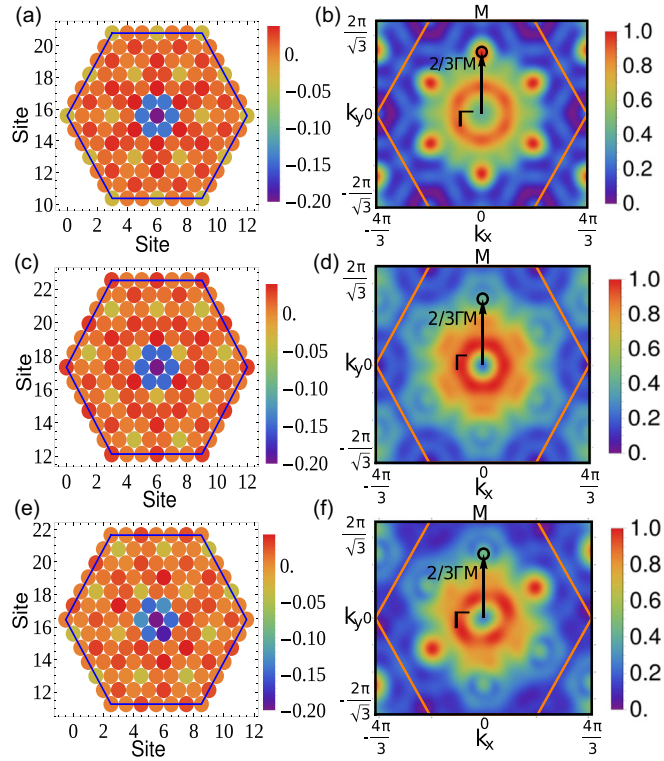

FIG. 4. Charge order map in real space in the presence of impurity [sitting at the center of each hexagon in (a), (c), and (e)] with impurity potential 0.5 eV for $V_{\mathrm{CDW}} = 0.02\,\mathrm{eV}$. The charge-order map and its Fourier transform are shown for (a),(b) sites of type 1; (c),(d) sites of type 2; and (e),(f) sites of type 3, respectively. The plotted region is zoomed in area near the impurity sites.

observables the configurational averaging would restore the D_{3h} symmetry relevant to monolayer $2H$-$NbSe_2$, the local breaking of symmetry can have interesting consequences in local observables including electron density variations near impurities or a locally observed superconducting gap in STM experiments. In Fig. 3(c) we show the density of states within an energy window of $\omega = \pm 30\,\mathrm{meV}$. This has been calculated by summing the site-resolved LDOS shown in Fig. 3(d) at $\omega = 20\,\mathrm{meV}$. For a $V_{\mathrm{CDW}} = 0.02\,\mathrm{eV}$, the corresponding LDOS gives a CDW gap of $\Delta_{\mathrm{CDW}} = 8\,\mathrm{meV}$ at the Fermi level that agrees well with previous work [7,48–50].

The suppression of the LDOS at Fermi energy is associated with the CDW gap and agrees well with similar features seen in the experiment [49]. The incomplete suppression implies that similar to bulk $2H$-$NbSe_2$, the CDW gap is highly anisotropic in momentum space. Another feature obtained in our calculations and observed in the previous STM experiments are the additional CDW-induced dips in LDOS at finite energies.

C. Effect of isolated impurities on CDW

To determine the interplay of CDW order and Ising spin-orbit coupling on the electronic structure of monolayer $2H$-$NbSe_2$, we study the perturbation of electronic properties near isolated impurities. The effect of a nonmagnetic impurity on the CDW is shown in Fig. 4. Here we show the impurity effect by considering a finite impurity potential of $V_{\mathrm{imp}} = 0.5\,\mathrm{eV}$ at the three different types of sites. The real-space electronic occupation around the impurity sites is shown in Fig. 4 on the left column, and the corresponding Fourier transform is shown in the right column. The Fourier transform clearly shows the expected symmetry of the local charge environment around the three different types of sites. For example, an impurity placed at site 1 or site 2 [see Figs. 4(a) and 4(c)] leads to a Fourier transform that has a sixfold rotational symmetry [Figs. 4(b) and 4(d)], whereas an impurity placed in site 3 clearly shows a Fourier transform with only a twofold rotational symmetry present [Figs. 4(e) and 4(f)]. In the case of a second type of impurity site, we see that the real-space [Fig. 4(c)] map does have a reduced D_{3h} symmetry, but the Fourier transform [Fig. 4(d)] remains approximately sixfold rotation symmetric since the symmetry breaking only contributes from lattice sites at larger distances from the impurity where the local charge-order modulation is already suppressed. It can also be seen that for impurity at site 2, the peak position in the Fourier transform does not show any significant peak at $2/3\Gamma M$, rather it shows high intensity near the Γ point indicating the formation of longer wavelength modulations. Similar self-consistent calculations with larger impurity potentials show a qualitatively similar but a more localized charge distribution.

To include the effect of strong magnetic fluctuations predicted in monolayer $2H$-$NbSe_2$, we next model the system close to a stoner magnetism by introducing a Hubbard-Kanamori Hamiltonian and tuning the Hubbard interaction ($U = 1.08$ eV, $J = U/4$) to lie close to the critical

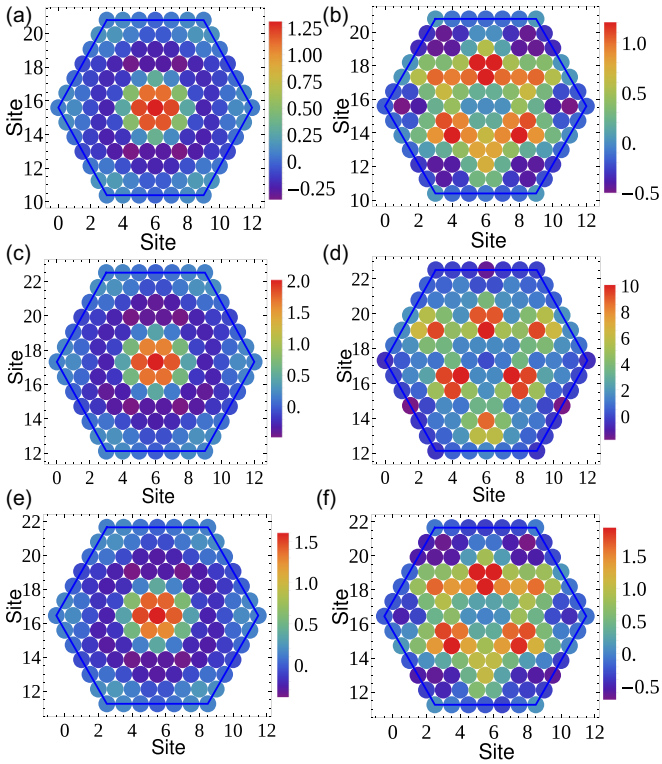

FIG. 5. Calculated magnetic moment $(n_{i\uparrow} - n_{i\downarrow})$ in the presence of impurity (sitting at the center of each hexagon) in the presence of Ising SOC (magnetic moments are in units of $10^{-3}/\mu_B$). The left and right columns represent an induced magnetic moment for a nonmagnetic impurity potential of 0.5 and 50 eV, respectively. (a),(b) Type 1 sites; (c),(d) type 2 sites; (e),(f) type 3 sites.

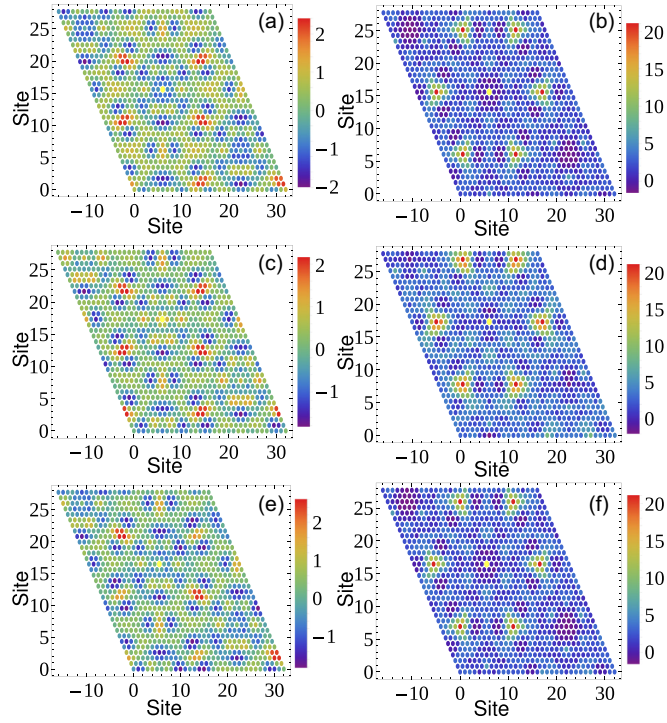

FIG. 6. Magnetic moment in the presence of nonmagnetic impurity (yellow dot in the middle of each plot) and in the absence of Ising SOC. The left and right columns represent the induced magnetic moment for a nonmagnetic impurity potential of 0.5 and 50 eV, respectively. (a),(b) Type 1 sites; (c),(d) type 2 sites; (e),(f) type 3 sites. In the left column, moments are in units of $10^{-6}/\mu_B$ (effectively zero), and in the right column, moments are in units of $10^{-3}/\mu_B$.

interaction strength ($U_c = 1.1$ eV). We do not find any qualitative differences in our results with small changes in the interaction parameter U.

Self-consistent calculation of the mean fields leads to a stabilization of local magnetization near the nonmagnetic impurity sites. In Fig. 5 we show the formation of the weak local magnetism near nonmagnetic impurities in the presence of an Ising spin-orbit coupling. Comparing Figs. 5(a) and 5(b), we find that the magnetic modulation near the impurity site has a longer correlation length for larger impurity strengths. This local modulation approximately maintains the lattice D_{3h} symmetry for impurity placed at the three types of sites shown in Figs. 5(b), 5(d), and 5(f). Interestingly, as shown in Fig. 6, impurity-induced magnetism computed in the absence of Ising spin-orbit coupling not only retains a local hexagonal D_{6h} symmetry for all three types of sites, but is significantly suppressed in magnitude and corresponds to a longer correlation length. The long lengthscale of the induced magnetic order in the absence of Ising SOC persists even in the absence of the underlying 3Q CDW order. We find that the additional lengthscale in the Friedel oscillations near the impurity induced by the Ising SOC localizes the magnetic moments closer to the impurity sites. We can therefore conclude that the presence of an Ising spin-orbit coupling enhances the tendency for the monolayer $NbSe_2$ to form local magnetism near disorder.

D. Effect on edge termination

The role of edge states in monolayer $2H$-$NbSe_2$ has been of interest because of the nontrivial topological nature of the material's electronic structure. Recent experiments find that the CDW order near the edge is significantly modified compared to the 3Q CDW pattern observed in the bulk regions [2]. In particular, it was proposed that the three-unit-cell modulation of the CDW order near the edge cannot be accounted for either via Friedel oscillations or quasiparticle interference effects. It has been argued to result from a superposition of the 3Q vectors of the CDW order near an edge. Here we study the effect of an edge using a realistic real-space self-consistent microscopic model that simulates the edge with open boundary conditions (Figs. 7 and 8).

We find a clear enhancement of electron occupation near the material edge with quasi-one-dimensional modulations of electron density [Figs. 7(b) and 7(d)]. The 3Q CDW ordering is restored as we move away from the edge towards its center [Figs. 7(a) and 7(c)]. Calculations of the orbital-resolved LDOS for d_{z^2} orbital at an energy $\omega = -17$ meV reveal the presence of stripe 1Q ordering as shown in Fig. 8(d). Such a modulation is weaker at the chemical potential and is further suppressed for positive energies $\omega = 17$ meV [Fig. 8(c)]. The orbital-resolved LDOS of the d_z^2 orbital is expected to dominate the differential conductance measured in STM experiments since the Wannier function corresponding to d_z^2

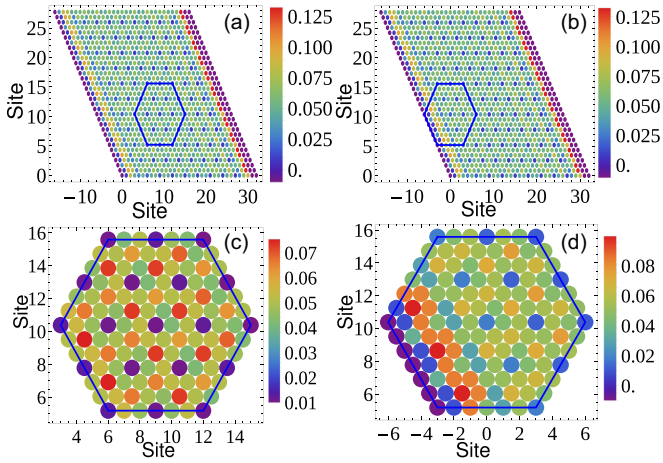

FIG. 7. Calculated charge ordering near a line edge: Plots (a), and (b) show the modulation of the CDW order parameter away from the edge with hexagonal marked regions that have been zoomed in (c), and (d) respectively.

orbitals will be more extended from the surface. In Figs. 8(c) and 8(d) we show the orbital-resolved LDOS for a $d_z{}^2$ orbital at energies $\omega = (17, -17)$ meV, respectively. It can be seen that a three-unit-cell stripe order is observed at around $\omega = -17$ meV, which gets suppressed at positive energies. Further, compared to the total LDOS shown at the same energies in Figs. 8(a) and 8(b), the three-unit-cell periodicity is much more apparent in the orbital-resolved LDOS. Similar energy-dependent modulation of the 1Q CDW order has been observed in STM experiments [2].

We next study the induced magnetic moment at the edge by considering open boundary conditions along the x direction,

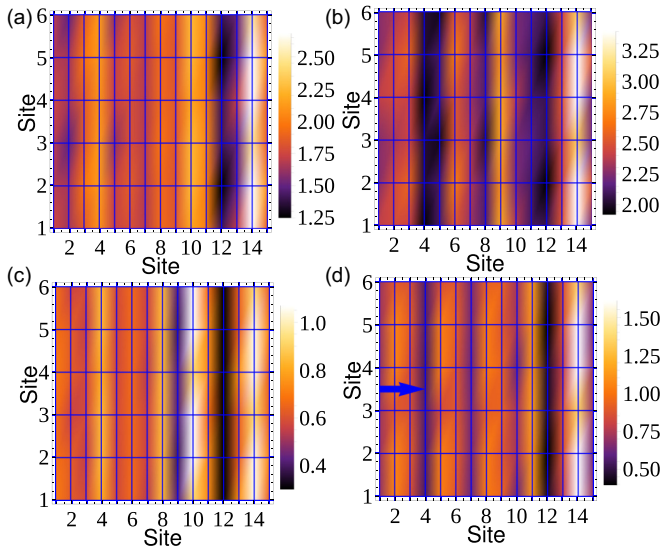

FIG. 8. Calculated LDOS for an open boundary along the x direction shown in Fig. 7. Parts (a) and (b) represent the LDOS plotted in a transverse direction from the edge summed over all three orbitals at energy 17 and -17 meV, respectively. Parts (c) and (d) show the LDOS contribution from d_{z^2} orbital at energy 17 and -17 meV, respectively.

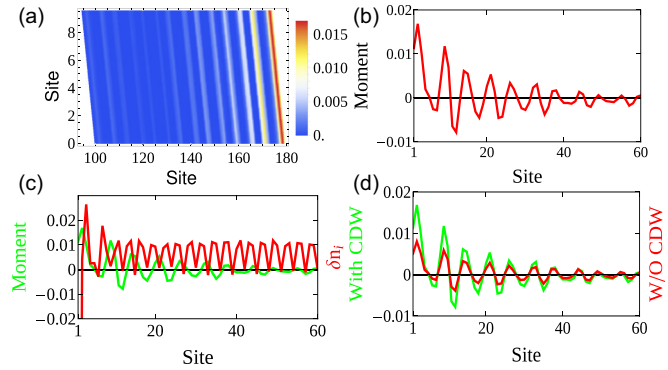

FIG. 9. Magnetic moment and charge ordering for $U = 1$ eV. (a),(b) Modulation of magnetic moment near an x-side edge. (c) Relative modulation of magnetic moment and charge ordering near the edge. (d) Enhancement of the induced magnetic order near the edge in the presence of a CDW order.

and strong paramagnetic fluctuations that place the system below but close to the stoner limit ($U < U_c$). In Fig. 9, we can see that there is a significant enhancement of magnetic moment localized near the edge [Figs. 9(a) and 9(b)]. As shown in Fig. 9(d), the induced moment near the edge is enhanced in the presence of a CDW order. This is due to the charge modulation induced by the CDW ordering that pushes certain sites closer to a local stoner instability, thus enhancing the induced magnetic moment. It can also be observed from Fig. 9(c) that the induced spin-density order near the edge has approximately twice the periodicity of the induced stripe charge order.

IV. CONCLUSION

The emergent order in a monolayer transition-metal dichalcogenide material like $2H$-$NbSe_2$ is expected to show interesting properties due to the interplay between charge ordering and an Ising spin-orbit coupling induced by the broken inversion symmetry. We find that the electronic structure of the material leads to a charge susceptibility that supports a 3Q CDW order at the $Q = 2/3\Gamma M$ wave vector under the influence of an anisotropic electronic phonon coupling. The Ising spin-orbit coupling plays only a weak role in the emergence of the charge order.

Further, self-consistent real-space mean-field calculations within a three-orbital model relevant to monolayer $2H$-$NbSe_2$, correctly stabilize the 3Q CDW order. It is found that nonmagnetic impurities lead to a charge order whose local modulation strongly depends on the interplay between the CDW and spin-orbit coupling. For example, in the presence of a CDW order, we distinguish three types of sites where the presence of an impurity could lead to a sixfold rotation symmetry, a threefold rotational symmetry, or a twofold symmetry of the local charge order depending upon the local environment around the impurities. In zero magnetic fields, the local symmetry breaking will be observable only in local probes like STM near the impurity or vacancy sites, as otherwise impurity averaging effects would restore the lattice symmetry. However, in the presence of a strong in-plane external magnetic field, the out-of-plane spins induced by the Ising SOC will

get canted, and any impurity averaging will not restore the lattice symmetry. This can lead to the breaking of the D_{3h} symmetry in global observables, and a twofold anisotropy can show up in measurements such as magnetoresistance. Similar twofold anisotropy of the superconducting gap structure has been observed in experiments in monolayer $NbSe_2$ [51].

By including electronic correlations in our calculations, we have studied the effects of recent predictions suggesting these monolayer materials are close to a magnetic instability. We find that local magnetic modulations can stabilize near non magnetic impurities with a triangular symmetry. Further, our calculations also reveal that the Ising spin-orbit coupling enhances the magnitude but significantly reduces the correlation lengthscale of these local moments.

Monolayer $2H$-$NbSe_2$ also undergoes interesting charge modulation near the edge of the material. We find the presence of a three unit cell 1Q charge ordering near the edge which is in agreement with recent experiments. These 1Q modulations exist for different types of edges in the presence of an underlying CDW instability in the lattice. Additionally, we also find the presence of a local stripe type magnetic ordering near the edge that has twice the periodicity as the underlying charge order modulations.

We believe that our work would be useful towards developing a better understanding of disorder effects, particularly in the context of local probe spectroscopy. The results would also be useful for developing an understanding of disorder effects within the superconducting state.

ACKNOWLEDGMENTS

S.M. acknowledges financial support by Science and Engineering Research Board (SERB), Department of Science and Technology, Ministry of Science and Technology, India through the MATRICS Grant No. MTR/2020/000524.

APPENDIX A: TIGHT-BINDING HAMILTONIAN

The low-energy tight-binding Hamiltonian for monolayer $2H$-$NbSe_2$ can be expressed as a sum of contributions from a three-orbital noninteracting Hamiltonian and a contribution that includes Ising SOC being given by $H = H_0 + H_{\rm SOC}$. The Hamiltonian terms can be expressed by

$$H_0 = \sum_{\mu\nu\sigma\boldsymbol{k}} H_{\mu\nu}(\boldsymbol{k}) c^{\dagger}_{\mu\sigma}(\boldsymbol{k}) c_{\nu\sigma}(\boldsymbol{k}), \tag{A1}$$

where the orbital index μ, ν and spin σ describe a d-orbital basis ($d_{z^2}, d_{xy}, d_{x^2-y^2}$). The Ising spin-orbit coupling contribution is given by

$$H_{\rm SOC} = it_{\rm SOC} \sum_{\boldsymbol{k}} [c^{\dagger}_{x^2-y^2\uparrow}(\boldsymbol{k}) c_{xy\uparrow}(\boldsymbol{k}) - c^{\dagger}_{x^2-y^2\downarrow}(\boldsymbol{k}) c_{xy\downarrow}(\boldsymbol{k})] + \text{Hermitian conjugate}. \tag{A2}$$

The elements of H_0 Hamiltonian are given by

$$\begin{aligned}
H_{11} &= e_1 + 2t_0[\cos(2k'_x) + 2\cos(k'_x)\cos(k'_y)] \\
&\quad + 2r_0[\cos(2k'_y) + 2\cos(3k'_x)\cos(k'_y)] + 2u_0[\cos(4k'_x) \\
&\quad + 2\cos(2k'_x)\cos(2k'_y)], \\
H_{12} &= -2\sqrt{3}t_2 \sin(k'_x)\sin k'_y + 2(r_1 + r_2)\sin(3k'_x) \\
&\quad \times \sin(k'_y) - 2\sqrt{3}u_2 \sin(2k'_x)\sin(2k'_y) + I\{2t_1 \sin(k'_x) \\
&\quad \times [2\cos(k'_x) + \cos(k'_y)] + 2(r_1 - r_2)\sin(3k'_x)\cos(k'_y) \\
&\quad + 2u_1 \sin(2k'_x)[2\cos(2k'_x) + \cos(2k'_y)]\}, \\
H_{13} &= 2t_2[\cos(2k'_x) - \cos(k'_x)\cos(k'_y)] \\
&\quad - \left(\frac{2}{\sqrt{3}}\right)(r_1 + r_2)[\cos(3k'_x)\cos(k'_y) - \cos(2k'_y)] \\
&\quad + 2u_2[\cos(4k'_x) - \cos(2k'_x)\cos(2k'_y)] \\
&\quad + I\left\{2t_1\sqrt{3}\cos(k'_x)\sin(k'_y)\right. \\
&\quad + \frac{2}{\sqrt{3}}\sin k'_y(r_1 - r_2)[\cos(3k'_x) + 2\cos(k'_y)] \\
&\quad \left. + 2\sqrt{3}u_1 \cos(2k'_x)\sin(2k'_y)\right\}, \\
H_{22} &= 2t_{11}\cos(2k'_x) + (t_{11} + 3t_{22})\cos(k'_x)\cos(k'_y) \\
&\quad + 4r_{11}\cos(3k'_x)\cos(k'_y) + 2(r_{11} + \sqrt{3}r_{12})\cos(2k'_y) \\
&\quad + (u_{11} + 3u_{22})\cos(2k'_x)\cos(2k'_y) + 2u_{11}\cos(4k'_x) \\
&\quad + e_2, \\
H_{23} &= [\sqrt{3}(t_{22} - t_{11})\sin(k'_x)\sin(k'_y) + 4r_{12}\sin(3k'_x) \\
&\quad \times \sin(k'_y) + \sqrt{3}(u_{22} - u_{11})\sin(2k'_x)\sin(2k'_y)] \\
&\quad + I\{4t_{12}\sin(k'_x)[\cos(k'_x) - \cos(k'_y)] \\
&\quad + 4u_{12}\sin(2k'_x)[\cos(2k'_x) - \cos(2k'_y)]\}, \\
H_{33} &= 2t_{22}\cos(2k'_x) + (3t_{11} + t_{22})\cos(k'_x)\cos(k'_y) \\
&\quad + 2r_{11}[2\cos(3k'_x)\cos(k'_y) + \cos(2k'_y)] + \frac{2}{\sqrt{3}}r_{12} \\
&\quad \times [4\cos(3k'_x)\cos(k'_y) - \cos(2k'_y)] + (3u_{11} + u_{22}) \\
&\quad \times \cos(2k'_x)\cos(2k'_y) + 2u_{22}\cos(4k'_x) + e_2.
\end{aligned}$$

The numerical values of the tight-binding matrix elements (Fig. 10) are given by

$$\begin{aligned}
&e_1 = 1.8247;\ e_2 = 2.07;\ t_0 = -0.12;\ t_1 = 0.3645; \\
&t_2 = 0.4449;\ t_{11} = 0.2068;\ t_{12} = 0.3498;\ t_{22} = -0.0961; \\
&r_0 = -0.036;\ r_1 = -0.025;\ r_2 = -0.0445;\ r_{11} = 0.071; \\
&r_{12} = 0.0285;\ u_0 = -0.034;\ u_1 = 0.0064;\ u_2 = 0.031; \\
&u_{11} = 0.087;\ u_{12} = 0;\ u_{22} = -0.054;\ t_{\rm SOC} = 0.075.
\end{aligned}$$

Here, $k'_x = \frac{1}{2}k_x a_{\rm lat}$ and $k'_y = \frac{\sqrt{3}}{2}k_y a_{\rm lat}$ (k_x and k_y are momentum space wave vectors and $a_{\rm lat}$ is the lattice constant).

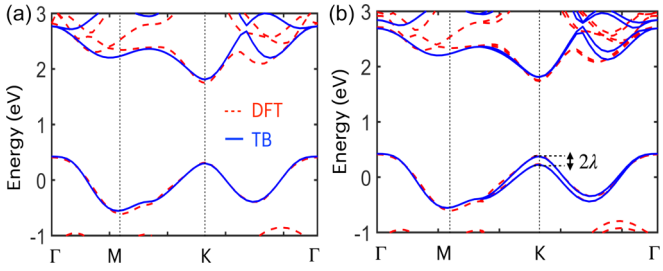

FIG. 10. DFT generated band structure (red dashed line) and the tight-binding fitting (blue line) of that in the absence of Ising SOC (left) and in the presence of Ising SOC (right).

APPENDIX B: MEAN-FIELD DECOUPLING

The Hubbard-Kanamori Hamiltonian expressed in an orbital basis can be given by

$$H_U = U\sum_{i,\mu}\hat{n}_{i\mu\uparrow}\hat{n}_{i\mu\downarrow} + U'\sum_{i,\mu\neq\nu}\sum_{\sigma}\hat{n}_{i\mu\sigma}\hat{n}_{i\nu\bar{\sigma}} + (U'-J)\sum_{i,\mu\neq\nu}\sum_{\sigma}\hat{n}_{i\mu\sigma}\hat{n}_{i\nu\sigma}. \tag{B1}$$

After performing a mean-field decomposition in the particle hole channel, it is given by

$$H_U = U\sum_{i,\mu}\langle n_{i\mu\uparrow}\rangle n_{i\mu\downarrow} + \langle n_{i\mu\downarrow}\rangle n_{i\mu\uparrow} + U'\sum_{i,\mu\neq\nu}\sum_{\sigma}\langle n_{i\mu\sigma}\rangle n_{i\nu\bar{\sigma}} + \langle n_{i\nu\bar{\sigma}}\rangle n_{i\mu\sigma} + (U'-J)\sum_{i,\mu\neq\nu}\sum_{\sigma}\langle n_{i\mu\sigma}\rangle n_{i\nu\sigma} + \langle n_{i\nu\sigma}\rangle n_{i\mu\sigma}. \tag{B2}$$

In the above expression, we have $U' = U - 2J$. The above mean-field form has been utilized in computing the local magnetic instability in the system. The CDW Hamiltonian originates from the e-ph interaction by integrating out the phonons. The quartic interaction term is restricted to the dominant isotropic contribution $[V_{\rm CDW}(\boldsymbol{k},\boldsymbol{Q}_m) = V_{\rm CDW}]$. The interaction Hamiltonian then reads

$$H_{\rm CDW} = V_{\rm CDW}\sum_{\substack{\mu,\nu,\gamma,\delta,\\ \boldsymbol{k},\boldsymbol{k}',m,\sigma}}\left(c^{\dagger}_{\mu,\boldsymbol{k},\sigma}c_{\nu,\boldsymbol{k}+\boldsymbol{Q}_m,\sigma}c^{\dagger}_{\gamma,\boldsymbol{k}',\sigma}c_{\delta,\boldsymbol{k}'-\boldsymbol{Q}_m,\sigma}\right). \tag{B3}$$

Fourier-transforming the above generates the corresponding Hamiltonian in real space,

$$H_{\rm CDW} = 2V_{\rm CDW}\sum_{\substack{\mu,\nu,\gamma,\delta\\ i,j,m,\sigma}}\cos\{\boldsymbol{Q}_m.(\boldsymbol{r}_i-\boldsymbol{r}_j)\}c^{\dagger}_{\mu i\sigma}c_{\nu i\sigma}c^{\dagger}_{\gamma j\sigma}c_{\delta j\sigma}. \tag{B4}$$

Further performing a mean-field decomposition, we define the CDW order parameter,

$$H_{\rm CDW} = \sum_{\substack{\mu,\nu,\gamma,\delta\\ j,m,\sigma}}\Delta^{m\sigma}_{\mu\nu}(r_j)c^{\dagger}_{\gamma j\sigma}c_{\delta j\sigma}, \tag{B5}$$

where

$$\Delta^{m\sigma}_{\mu\nu}(\boldsymbol{r}_j) = 2V_{\rm CDW}\sum_{i}\cos\{\boldsymbol{Q}_m.(\boldsymbol{r}_i-\boldsymbol{r}_j)\}\langle c^{\dagger}_{\mu i\sigma}c_{\nu i\sigma}\rangle. \tag{B6}$$

As discussed above, the order parameter is restricted to site-ordered terms.

[1] X. Xi, L. Zhao, Z. Wang, H. Berger, L. Forró, J. Shan, and K. F. Mak, Nat. Nanotechnol. **10**, 765 (2015).
[2] Q. Zhang, J. Fan, T. Zhang, J. Wang, X. Hao, Y.-M. Xie, Z. Huang, Y. Chen, M. Liu, L. Jia *et al.*, Commun. Phys. **5**, 117 (2022).
[3] R. Bianco, L. Monacelli, M. Calandra, F. Mauri, and I. Errea, Phys. Rev. Lett. **125**, 106101 (2020).
[4] C.-S. Lian, C. Si, and W. Duan, Nano Lett. **18**, 2924 (2018).
[5] Y.-T. Hsu, A. Vaezi, M. H. Fischer, and E.-A. Kim, Nat. Commun. **8**, 14985 (2017).
[6] M. Calandra, I. I. Mazin, and F. Mauri, Phys. Rev. B **80**, 241108(R) (2009).
[7] D. Wickramaratne, S. Khmelevskyi, D. F. Agterberg, and I. I. Mazin, Phys. Rev. X **10**, 041003 (2020).
[8] H. Mutka, Phys. Rev. B **28**, 2855 (1983).
[9] U. Chatterjee, J. Zhao, M. Iavarone, R. Di Capua, J. Castellan, G. Karapetrov, C. Malliakas, M. G. Kanatzidis, H. Claus, J. Ruff *et al.*, Nat. Commun. **6**, 6313 (2015).
[10] F. Flicker and J. Van Wezel, Nat. Commun. **6**, 7034 (2015).
[11] F. Flicker and J. van Wezel, Phys. Rev. B **94**, 235135 (2016).
[12] H. Wang, X. Huang, J. Lin, J. Cui, Y. Chen, C. Zhu, F. Liu, Q. Zeng, J. Zhou, P. Yu *et al.*, Nat. Commun. **8**, 394 (2017).
[13] C. M. Varma, E. I. Blount, P. Vashishta, and W. Weber, Phys. Rev. B **19**, 6130 (1979).
[14] S. Kim and Y.-W. Son, Phys. Rev. B **96**, 155439 (2017).
[15] D. Sticlet and C. Morari, Phys. Rev. B **100**, 075420 (2019).
[16] G.-B. Liu, W.-Y. Shan, Y. Yao, W. Yao, and D. Xiao, Phys. Rev. B **88**, 085433 (2013).
[17] C. Wang, B. Lian, X. Guo, J. Mao, Z. Zhang, D. Zhang, B.-L. Gu, Y. Xu, and W. Duan, Phys. Rev. Lett. **123**, 126402 (2019).
[18] M. R. Aliabad and M.-H. Zare, Phys. Rev. B **97**, 224503 (2018).
[19] E. Sohn, X. Xi, W.-Y. He, S. Jiang, Z. Wang, K. Kang, J.-H. Park, H. Berger, L. Forró, K. T. Law, J. Shan and K. F. Mak, Nat. Mater. **17**, 504 (2018).
[20] M. Gupta, A. Chauhan, S. Satpathy, and B. R. K. Nanda, Phys. Rev. B **108**, 075139 (2023).
[21] M. D. Johannes and I. I. Mazin, Phys. Rev. B **77**, 165135 (2008).
[22] N. Doran, D. Titterington, B. Ricco, M. Schreiber, and G. Wexler, J. Phys. C **11**, 699 (1978).
[23] M. D. Johannes, I. I. Mazin, and C. A. Howells, Phys. Rev. B **73**, 205102 (2006).
[24] D. W. Shen, Y. Zhang, L. X. Yang, J. Wei, H. W. Ou, J. K. Dong, B. P. Xie, C. He, J. F. Zhao, B. Zhou, M. Arita, K. Shimada, H. Namatame, M. Taniguchi, J. Shi, and D. L. Feng, Phys. Rev. Lett. **101**, 226406 (2008).

[25] Z. Wang, C. Chen, J. Mo, J. Zhou, K. P. Loh, and Y. P. Feng, Phys. Rev. Res. **5**, 013218 (2023).
[26] Y. Nakata, K. Sugawara, S. Ichinokura, Y. Okada, T. Hitosugi, T. Koretsune, K. Ueno, S. Hasegawa, T. Takahashi, and T. Sato, npj 2D Mater. Appl. **2**, 12 (2018).
[27] E. Liebhaber, S. Acero González, R. Baba, G. Reecht, B. W. Heinrich, S. Rohlf, K. Rossnagel, F. von Oppen, and K. J. Franke, Nano Lett. **20**, 339 (2020).
[28] M. Ruby, B. W. Heinrich, Y. Peng, F. von Oppen, and K. J. Franke, Phys. Rev. Lett. **120**, 156803 (2018).
[29] R. Pervin, M. Krishnan, A. Sonachalam, and P. M. Shirage, J. Mater. Sci. **54**, 11903 (2019).
[30] F. Cossu, A. G. Moghaddam, K. Kim, H. A. Tahini, I. Di Marco, H.-W. Yeom, and A. Akbari, Phys. Rev. B **98**, 195419 (2018).
[31] K. Cho, M. Kończykowski, S. Teknowijoyo, M. A. Tanatar, J. Guss, P. Gartin, J. Wilde, A. Kreyssig, R. McQueeney, A. I. Goldman *et al.*, Nat. Commun. **9**, 2796 (2018).
[32] A. Skripov and A. Stepanov, Solid State Commun. **53**, 469 (1985).
[33] C. D. Malliakas and M. G. Kanatzidis, J. Am. Chem. Soc. **135**, 1719 (2013).
[34] A. Soumyanarayanan, M. M. Yee, Y. He, J. Van Wezel, D. J. Rahn, K. Rossnagel, E. Hudson, M. R. Norman, and J. E. Hoffman, Proc. Natl. Acad. Sci. USA **110**, 1623 (2013).
[35] D. Moncton, J. Axe, and F. DiSalvo, Phys. Rev. Lett. **34**, 734 (1975).
[36] L. Cai, J. He, Q. Liu, T. Yao, L. Chen, W. Yan, F. Hu, Y. Jiang, Y. Zhao, T. Hu *et al.*, J. Am. Chem. Soc. **137**, 2622 (2015).
[37] R. B. Christensen, P. J. Hirschfeld, and B. M. Andersen, Phys. Rev. B **84**, 184511 (2011).
[38] Y. Chen and C. S. Ting, Phys. Rev. Lett. **92**, 077203 (2004).
[39] J. H. J. Martiny, A. Kreisel, and B. M. Andersen, Phys. Rev. B **99**, 014509 (2019).
[40] B. M. Andersen, P. J. Hirschfeld, A. P. Kampf, and M. Schmid, Phys. Rev. Lett. **99**, 147002 (2007).
[41] Z. Wang and P. A. Lee, Phys. Rev. Lett. **89**, 217002 (2002).
[42] J. A. Robertson, S. A. Kivelson, E. Fradkin, A. C. Fang, and A. Kapitulnik, Phys. Rev. B **74**, 134507 (2006).
[43] P. E. Blöchl, Phys. Rev. B **50**, 17953 (1994).
[44] G. Kresse and J. Furthmüller, Phys. Rev. B **54**, 11169 (1996).
[45] G. Kresse and D. Joubert, Phys. Rev. B **59**, 1758 (1999).
[46] H. K. Kundu, S. Ray, K. Dolui, V. Bagwe, P. R. Choudhury, S. B. Krupanidhi, T. Das, P. Raychaudhuri, and A. Bid, Phys. Rev. Lett. **119**, 226802 (2017).
[47] G. Gómez-Santos and F. Ynduráin, Phys. Rev. B **29**, 4459 (1984).
[48] J. Á. Silva-Guillén, P. Ordejón, F. Guinea, and E. Canadell, 2D Mater. **3**, 035028 (2016).
[49] M. M. Ugeda, A. J. Bradley, Y. Zhang, S. Onishi, Y. Chen, W. Ruan, C. Ojeda-Aristizabal, H. Ryu, M. T. Edmonds, H.-Z. Tsai *et al.*, Nat. Phys. **12**, 92 (2016).
[50] F. Zheng, Z. Zhou, X. Liu, and J. Feng, Phys. Rev. B **97**, 081101(R) (2018).
[51] E. Khestanova, J. Birkbeck, M. Zhu, Y. Cao, G. Yu, D. Ghazaryan, J. Yin, H. Berger, L. Forro, T. Taniguchi *et al.*, Nano Lett. **18**, 2623 (2018).